CFL1-dependent dynamicity of surface ectoderm filopodia-like protrusions enhances neurulation zippering speed in mice

Abigail R Marshall[1], Andrea Krstevski[1], Henry Croswell[1], Rahul Shah[1], Eirini Maniou[1,2], Nicholas DE Greene[1], Andrew J Copp[1], Gabriel L Galea[1,*]

1. Developmental Biology and Cancer, UCL GOS Institute of Child Health, 30 Guilford Street, London, WC1N 1EH, UK
2. Department of Industrial Engineering, University of Padova, Padova, 35131, Italy

* Corresponding author, g.galea@ucl.ac.uk

Abstract

Progression of caudally-directed embryonic neural tube closure must exceed that of body axis elongation, otherwise closure is incomplete and neural tube defects arise. Genetic deletion and pharmacological antagonism studies establish the critical role of actomyosin regulation in this closure process in mice, but many models of impaired F-actin regulation are limited by early embryonic lethality, which precludes mechanistic insight *in vivo*. Here, we test the physiological functions of the F-actin severing protein CFL1 by selective deletion in various tissues of mouse embryos undergoing neural tube closure. Loss of CFL1 in the cranial neuroepithelium diminishes selective apical localisation of F-actin and produces dysmorphic, asymmetrical headfolds which fail to meet at the dorsal midline, causing exencephaly, with partial penetrance. During spinal neurulation, neuroepithelial CFL1 is dispensable, but its expression in the surface ectoderm enhances the dynamicity of filopodia-like protrusions involved in the zippering process of midline epithelial fusion. Compared with littermate controls, spinal zippering speed is decreased by 30% in embryos lacking surface ectoderm CFL1 and approximately 30% of embryos develop spina bifida. These findings suggest that molecular-level cytoskeletal regulation by CFL1 sets the cellular-level dynamicity of filopodial extensions which limit tissue-level zippering speed necessary to fully close the neural tube.

Key words:

CFL1, neural tube, spina bifida, filopodia, mouse

Introduction

Embryonic morphogenesis requires biochemical inputs which produce cellular mechanical outputs to predictably change tissue shape and form functional organs. Cellular generation of mechanical force often depends on coordinated regulation of the actomyosin cytoskeleton. Myosin activation, such as through Rho/ROCK signalling, generates contractile forces which are transmitted between cells through F-actin anchored to cell-cell junctions. F-actin is itself polymerised through the action of formin and ARP2/3 complexes, stabilised by various binding proteins and destabilised by severing proteins including the non-muscle cofilin, CFL1(1, 2). The intricate interplay between these processes has largely been discovered thanks to elegant studies using *in vitro* reactions or cultured cells (3-5), particularly in the context of cellular extension of lamellipodia and filopodia during migration (6-9). The relevance of these processes *in vivo* has been clearly demonstrated in tractable model organisms and morphogenetic events, such as *Drosophila* dorsal closure (10). Genetic variants of many actomyosin regulators, including *CFL1* (11), have also been implicated in human disease. However, analysis of their functions during mammalian morphogenesis has been hindered by the redundancy of many factors (12), or early embryonic lethality when non-redundant genes are disrupted (13). Here, we use conditional gene deletion approaches in mice to mechanistically dissect non-redundant cellular functions of CFL1 during mammalian neurulation.

Neurulation is the morphogenetic process by which vertebrate embryos form the neural tube, the embryonic precursor of the central nervous system (14). In mice, as in humans, neural tube closure initiates at distinct closure points where the neuroepithelium is initially bent dorsally, elevating its lateral margins such that they are brought together at the dorsal midline (15, 16). As the left and right halves approach each other, the overlying surface ectoderm fuses and zippers along the length of the embryo. This sequence of elevation, apposition and zippering propagates away from the closure-initiating points until the neural tube is fully closed along the

length of the embryo. The speed at which closure progresses must exceed the rate of growth and body axis elongation, on which it is superimposed. If not, part of the neural tube fails to close such that neural tissue remains exposed on the outside of the body, as occurs in spina bifida.

We and others have demonstrated that failure of the neuroepithelium to bend or elevate (17-19), or of the surface ectoderm to zipper (15, 20), can each cause spina bifida in mice. Diminution of actomyosin contraction, for example by pharmacologically antagonizing ROCK activation (17, 21) or genetic disruption of its up-stream activation by planar cell polarity signalling in the neuroepithelium (18), stops elevation of the spinal neural folds in the posterior neuropore (PNP). Surface ectoderm actomyosin also mechanically contributes to closure of the PNP, including through contraction of high-tension actomyosin cables which run along the neural folds (22, 23). Surface ectoderm cells are responsible for establishing the first, delicate contacts between the left and right neural fold tips at the dorsal midline (13, 24). They do so by extending cellular protrusions into the fluid-filled space ahead of them to establish new contacts with their contralateral partners, likely by first forming nascent cell-ECM contacts which mature into stable cell-cell contacts (20). The nature of the protrusions they extend changes at different levels of spinal closure (13). At cervical and high thoracic levels, they predominantly form filopodial-like protrusions under the control of the small GTPase CDC42 (13). Later in development, and lower down the body, they also form broader lamellipodia-like ruffles which require a different GTPase, RAC1 (13). Differential regulation of filopodia by CDC42 and lamellipodia by RAC1 is well-established in vitro (25).

CDC42/RAC1 commonly act in opposition to Rho GTPases such as RHOA during epithelial morphogenesis (25-28). Their antagonistic effects are neatly demonstrated in the growth cone F-actin of neural axons, where CDC42/RAC1 promote axonal extension whereas RHO activation causes growth cone collapse and retraction (29). Their relative activities are carefully

balanced, at least in part through regional localisation within each cell. For example, CDC42 and RHOA activation can each result in inhibition of CFL1 through phosphorylation by LIM kinase (LIMK) (30-32), but local antagonism of RHOA by CDC42 can result in a net increase of CFL1 activity leading to increases in the length and number of filopodia (33).

CFL1 has both obligate and redundant roles with other F-actin severing proteins such as actin depolymerising factor (ADF)/destrin (11). Its non-redundant roles are clearly illustrated by the embryonic lethality, during neural tube closure, when it is genetically deleted in mice despite up-regulation of ADF (34). Global *Cfl1* knockout mouse embryos have defective neural crest migration, diminished apical localisation of neuroepithelial actomyosin, fully penetrant failure of cranial neural tube closure causing exencephaly, and longer PNPs than somite stage-matched wildtype embryos suggesting predisposition to spina bifida (21, 34, 35). *CFL1* genetic variants have also previously been associated with increased spina bifida risk in humans (36, 37). However, global developmental delay and the likely multiplicity of CFL1 functions in different tissues limit the use of global knockout embryos for mechanistic studies into its non-redundant functions in different cell types.

A well-established method of identifying cell-specific consequences of gene loss of function in vivo is conditional deletion using tissue-specific Cre recombinase expression. Several Cre-drivers are known to drive gene deletion in either the surface ectoderm or neuroepithelium during neurulation. For example, we and others have extensively used *Grhl3*^{Cre} to robustly delete genes of interest throughout the surface ectoderm flanking the spinal neural tube, and mosaically in some neuroepithelial cells, starting shortly before the onset of neurulation (13, 19, 20, 38). Here, we use a combination of Cre-drivers to identify tissue-specific roles of CFL1 during mouse primary neurulation with a focus on spinal closure. We show that CFL1 facilitates spinal zippering by increasing dynamicity of filopodia-like protrusions from the surface ectoderm leading edge.

Results

CFL1 is regionally enriched and inhibited in the surface ectoderm and neuroepithelium

CFL1 is ubiquitously present in the surface ectoderm and neuroepithelium of mouse embryos undergoing primary neurulation (Figure 1A). In the spinal region, CFL1 is particularly prominent at the leading edge of surface ectoderm cells immediately caudal to the zippering point (Figure 1A, quantified in Supplementary Figure 1A-B). The phosphorylated, inhibited form of CFL1 (pCFL1) is particularly enriched in midline surface ectoderm cells. In the cranial region, cells with abundant pCFL1 line the open neural folds and are present along the recently-fused midline seam (Figure 1B). In the spinal region, equivalent pCFL1-enriched cells are not observed lining the open neuropore, but are visible along the recently-closed midline when the surface ectoderm is selectively visualised without signal from deeper tissues (Figure 1C-D and Supplementary Figure 1C-D). Surface visualisation also emphasises diminished pCFL1 in mitotic cells of both the surface ectoderm and neuroepithelium (Figure 1C).

The midline enrichment of pCFL1 corresponds to a region of enhanced F-actin staining intensity (Supplementary Figure 1C-D) and previously-reported prominent phosphorylation of the ROCK target pMLC2 (15). ROCK1 immunolocalises around midline surface ectoderm cell borders (Figure 1E) and pharmacological blockade of RHO/ROCK signalling globally reduces pCFL1 staining intensity (Figure 1F-G). Taken together, the localisation pattern of total and inactive CFL1 suggests dynamic activation related to cytoskeletal regulation downstream of RHO/ROCK signalling, particularly in surface ectoderm cells involved in midline fusion during mouse neurulation. During spinal zippering, active CFL1 is selectively enriched along the neuropore-facing border of surface ectoderm cells which are yet to fuse along the embryonic midline, and is then phosphorylated (inhibited) once these cells have completed their zippering function.

Conditional deletion of *Cfl1* causes partially-penetrant neural tube defects

Global deletion of *Cfl1* has previously been reported to cause fully penetrant exencephaly attributed at least in part to dysregulation of actomyosin apical localisation (21, 35). To circumvent early lethality, we conditionally deleted *Cfl1* with Cre expressed from the *Grhl3* locus. Embryos lacking *Cfl1* in the *Grhl3*^{Cre} domain (henceforth Cre;Fl/Fl) develop partially penetrant neural tube defects (Figure 2A-B), including exencephaly, spina bifida, and kinked tail phenotypes (indicative of delayed PNP closure). No phenotypes are observed in embryos lacking one copy of *Cfl1* in the *Grhl3*^{Cre} domain (Cre;Fl/+, Figure 2A-B) and these have subsequently been included with Cre-negative embryos as controls.

Exencephaly is caused by failed cranial neural tube closure. We observe a subset of Cre;Fl/Fl embryos which fail to elevate and appose the neural folds at the embryonic midline between the forebrain and midbrain, where Closure 2 forms (Supplementary Figure 2A-B). During these stages of neural fold elevation, we reliably detect mosaic loss of CFL1 in the neuroepithelium, whereas the protein remains abundantly present in the surface ectoderm (Supplementary Figure 2C-D). Mosaic neuroepithelial loss of CFL1 is consistent with expression of *Grhl3* in the cranial neuroepithelium at these stages of closure (39). Neuroepithelial loss of CFL1 is evident at very early stages of headfold elevation (e.g. 3-4 somite stages, Supplementary Figure 2D). It does not result in overall changes in neuroepithelial apical area, proliferation, or apoptosis, such that abnormalities in these behaviours are unlikely to explain tissue-level failure of neural fold elevation (Supplementary Figure 2E-I).

Mosaic CFL1 loss in the cranial neuroepithelium impairs selective localisation of F-actin apically (Supplementary Figure 3A-B). Baso-laterally enriched F-actin appears cell-autonomously associated with individual cells mosaically lacking CFL1 (Supplementary Figure 3C), but is sufficiently marked to increase basolateral F-actin intensity across the tissue relative to control embryos (Supplementary Figure 3B). Coordinated actomyosin contraction normally produces

predictable changes in cranial neural fold shape (40-43) and previous work described irregular or convoluted folding of the cranial neural tube in embryos with impaired actomyosin activation (44). We similarly observe highly dysmorphic cranial neural folds in Cre;Fl/Fl embryos (Supplementary Figure 3D). To quantify this dysmorphology, we compared discrepancy in projected area between the left and right neural folds, showing that Cre;Fl/Fl cranial neural folds are less accurately matched to each other than in controls (Supplementary Figure 3E). These findings suggest coordinated F-actin localisation is required for symmetrical tissue shapes, presumably facilitating symmetrical elevation and fusion of the neural folds to form Closure 2. This is consistent with previous observations in *Xenopus* studying mosaic deletion of different F-actin regulators (45).

Neuroepithelial *Cfl1* is dispensable for spinal neural tube closure

Unlike in the forebrain/midbrain region at early closure stages, in the spinal neural tube *Grhl3*^{Cre} robustly deletes *Cfl1* in the surface ectoderm throughout closure, as well as in a subset of neuroepithelial cells (Figure 2C-E). Its loss in either, or both, of these tissues could cause failure of neuropore closure. We propose that quantifiable abnormalities in PNP morphological features can be used to identify deficiencies in the cellular processes normally responsible for achieving those shapes. For example, we previously reported that *Grhl3*^{Cre} deletion of a different gene, *Vangl2,* initially impairs neural fold elevation through neuroepithelial apical constriction (18, 19). *Grhl3*^{Cre}-mediated gene deletion can also cause spina bifida by impairing surface ectoderm zippering, such as in the case of deleting *Itgb1* (20).

Here, we compare morphometric analysis of neuropores from embryos within the 20-25 somite range in which *Grhl3*^{Cre} is used to cause partially-penetrant spina bifida by deleting *Cfl1*, *Vangl2*, or *Itgb1*. At this developmental stage, conditional *Cfl1* deletion significantly increases PNP

length (Figure 2F), without altering width (Figure 2G) or neural fold elevation (Figure 2H). This contrasts with equivalent deletion of neuroepithelially-active *Vangl2*, which increases width and diminishes elevation before impacting neuropore length (Supplementary Figure 4A). It is more consistent with the shape abnormalities seen when the surface ectoderm-active *Itgb1* is deleted, causing an increase in neuropore length with less pronounced changes in width, although we also observe paradoxically increased neural fold elevation in the *Itgb1* model (Supplementary Figure 4B). All three of these *Grhl3*^{Cre}-mediated gene deletion models cause partially penetrant spina bifida, but the neuropore dysmorphologies resulting in failure of closure are gene-specific.

Identifying neuropore length as the earliest PNP abnormality in the *Cfl1* model suggests a primary failure of the surface ectoderm mechanisms responsible for zippering. Increased neuropore length in Cre;Fl/Fl embryos is observed at even earlier stages of development than the 20-25 somite range used to compare models (Supplementary Figure 4C). However, neither morphometric analysis nor protein localisation exclude non-redundant roles for neuroepithelial CFL1 in spinal neurulation. To test this, we initially used inducible *T*^{CreERT2} to mimic the pattern of *Grhl3*^{Cre} recombination mosaically in the neuroepithelium (and mesoderm), but without recombination in the surface ectoderm. Tamoxifen-induced activation of *T*^{CreERT2} induces early and persistent recombination (Figure 3A-B), resulting in mosaic loss of CFL1 in the spinal neuroepithelium by E9.5 (Figure 3C). *T*^{CreERT2} deletion of *Cfl1* does not cause spina bifida or kinked tail phenotypes, even when one allele of *Cfl1* is pre-deleted (*T*$^{CreERT2/+}$*Cfl1*$^{Fl/-}$ embryos, Figure 3D). Paradoxically, a subset of *T*$^{CreERT2/+}$*Cfl1*$^{Fl/-}$ embryos have exencephaly (Figure 3D) despite lack of cranial recombination (Figure 3A). This could be due to a gene/gene interaction or haploinsufficiency when one allele of *Cfl1* is lost. We generated *Cfl1*$^{+/-}$ embryos, and observed an equivalent penetrance of exencephaly (Supplementary Figure 5A-B), supporting a haploinsufficiency phenotype.

To further test potential non-redundant roles of *Cfl1* in the neuroepithelium during spinal closure we additionally deleted this gene using *Cdx2*^{Cre}. *Cdx2*^{Cre} recombines exclusively in the spinal neuroepithelium at early stages of neural tube closure, before recombining in the surface ectoderm and mesoderm at later and more caudal stages (Figure 3E). This produces a region of primarily spinal cord recombination along the thorax before expanding to other tissues (Figure 3F). Consequently, *Cdx2*^{Cre} deletes *Cfl1* initially in the neuroepithelium (Figure 3G), then more globally in all tissues at later stages and corresponding to more caudal anatomical locations (Figure 3H), later than the developmental stages when *Grhl3*^{Cre} deletion of *Cfl1* produces longer neuropores. *Cdx2*^{Cre} deletion of *Cfl1* produces a low penetrance of kinked tail, suggesting delayed neuropore closure, but no embryos with spina bifida are observed (Figure 3I-J).

These alternative Cre-mediated deletions reinforce protein localisation and morphometric analyses which suggest that surface ectoderm roles of CFL1 underlie spina bifida in the *Grhl3*^{Cre}*Cfl1*$^{Fl/Fl}$ model. *Grhl3*^{Cre} is used in the remainder of the manuscript.

Surface ectoderm deletion of *Cfl1* alters cellular F-actin, shape and apoptosis

We previously identified supracellular, high-tension F-actin cables assembled by the surface ectoderm leading edge which facilitate neuropore closure (17, 22). These cables remain present in Cre;Fl/Fl embryos (Figure 4A). We used laser ablation, as previously reported (17, 23), to functionally test the tension withstood by these cables (Supplementary Figure 6A). Recoil following cable ablation tended to be less variable in Cre;Fl/Fl compared with control embryos (Levene's test $p = 0.09$) but was not significantly different from, and entirely within the physiological range observed in, control embryos (Supplementary Figure 6B). Similarly, recoil following ablation of surface ectoderm cell borders away from the cables does not differ significantly between Cre;Fl/Fl and control embryos (Supplementary Figure 6C).

Analysis of surface ectoderm F-actin structures is complicated by super-imposition of the basal surface ectoderm on the basal neuroepithelium over an irregular surface (Figure 4A), making it difficult to separate them in *en face* imaging. We used surface subtraction to selectively visualise F-actin in different cellular sub-domains (schematically illustrated below Figure 4B-C). As previously observed *in vitro* (46), *Cfl1*-depleted cells have more prominent stress fibre-like arrangements than those observed in controls (Figure 4B). Closer to the basal domain, Cre;Fl/Fl embryos appear to have sparser but longer F-actin fibres than controls (Figure 4C). We therefore analysed cell shape as a functional readout of cytoskeletal disruption. Midline surface ectoderm cells in Cre;Fl/Fl embryos appear larger (Figure 4D-E) and have more concave cell borders which result in reduced shape 'solidity' (Figure 4F) than those in control embryos. Shape index, a computed measure of epithelial fluidity, is not significantly different between genotypes (Supplementary Figure 6D) and neither is their mitotic index (Supplementary Figure 6E-F). However, Cre;Fl/Fl embryos frequently have prominent apoptotic bodies within the surface ectoderm over the dorsal midline: these are also observed in control embryos but are abnormally large in those lacking surface ectoderm *Cfl1* (Supplementary Figure 6E). The apoptotic bodies are located rostral to the advancing zippering point, and we consider them unlikely to be responsible for failure of zippering.

Loss of surface ectoderm CFL1 diminishes zippering rate and filopodial dynamics

Previous studies demonstrated that CDC42-dependent filopodia-like protrusions from surface ectoderm cells initiate spinal zippering at early stages of neuropore closure, before RAC1-dependent lamellipodia-like ruffles become more prominent later (13). Both types of protrusions co-occur during the intermediate closure period, when the thoracic spinal cord is formed. The protrusions are readily visible in reflection imaging of 15-20 somite stage embryos (Figure 5A). Thin filopodia-like protrusions are more abundant in Cre;Fl/Fl embryos than controls (Figure

5B), whereas lamellipodia-like ruffles are less numerous and observed similarly in both genotypes (Control = 0.85±0.15 ruffles/100 µm, Cre;Fl/Fl = 0.78±0.16 ruffles/100 µm, mean±SEM, analysed in the same embryos as in Figure 5B).

Surface ectoderm protrusive activity normally ceases abruptly as cells leave the leading edge of the open neuropore and come to overlie the most recently closed portion of neural tube. However, in a subset of Cre;Fl/Fl embryos, a region of persistent protrusive activity is observed along the embryonic midline where closure has occurred (Figure 5C-D). To test whether these protrusions come from the surface ectoderm or the underlying neuroepithelium we generated Cre;Fl/Fl embryos with an EGFP lineage trace of *Grhl3*^{Cre}. This showed a small number of filopodia-like membrane protrusions in Cre;Fl/+ embryos, which are markedly increased in Cre;Fl/Fl embryos with persistent midline protrusions (Figure 5E).

This analysis excludes absence of either lamellipodial or filopodial-type protrusions as the cause of spina bifida in our conditional *Cfl1* deletion model, but raises the possibility that excess filopodia may be produced as a compensatory mechanism to increase zippering if other mechanisms are deficient. To directly assess the speed of zippering, we used our previously-reported method (15) in which DiI crystals are injected under the surface ectoderm at the level of the zippering point, then embryos are cultured to quantify their closure rate by measuring the distance of the zippering point from the DiI labelling site prior to culture (Figure 5F). Cre;Fl/Fl embryos zipper at a significantly slower rate than controls (Figure 5G). Neither control nor Cre;Fl/Fl zippering rate distributions differ significantly from statistical normality, suggesting an overall reduction of zippering rate in the Cre;Fl/Fl embryos with a subset failing to achieve closure prior to a morphogenetic deadline, rather than failure of zippering in a subgroup of embryos.

To establish the sub-cellular basis of slower zippering rate in embryos lacking *Cfl1* in the surface ectoderm, we performed live-imaging of zippering protrusions. Given zippering

protrusions had not previously been live-imaged in the PNP, we initially confirmed that surface ectoderm cells on either side of the midline gap produce dynamic protrusions which meet at the embryonic midline and fuse (Figure 6A), as had previously been inferred from static images in the PNP and live-imaged in the hindbrain neuropore (24, 44). Both narrow filopodia-like protrusions and broader lamellipodia-like ruffles dynamically reach beyond the epithelial surface ectoderm cells into the space ahead of them at the zippering point and along the open neural folds (Figure 6A). In pilot studies using wild-type embryos we observed that lamellipodial-type ruffles are relatively stable features, constantly changing their shape but identifiable for long periods of time over many minutes (Figure 6A). In contrast, filopodial-type protrusions are ephemeral, rapidly forming, deforming and regressing over a few minutes (Figure 6A).

Given we primarily observe increased filopodial-type protrusions in Cre;Fl/Fl embryos, we visualised the zippering point over a short, 5-minute period. The majority of filopodial-type protrusions in control embryos are only visible for a 1-2 minute period before regressing, with only a small subset (16%) being visible for the full five-minute interval (Figure 6B). In Cre;Fl/Fl embryos, these protrusions typically persisted for longer periods of time with over half (59%) of observed protrusions present throughout the 5-minute imaging period (Figure 6B). Filopodial protrusions in control embryos changed angle extensively between 15 second timesteps, consistent with their exploratory behaviour, whereas those lacking *Cfl1* had smaller changes in angle (Figure 6C).

We previously reported that surface ectoderm protrusions use integrin B1-dependent ECM attachments, likely to fibronectin, to establish initial connections across the embryonic midline (20). These nascent cell-ECM-cell connections are required for surface ectoderm cells at the zippering point to constrict their neuropore-facing cell border and leave the zippering point along the embryonic midline (20) (Figure 6D-E), as was initially observed in *Ciona* (47). Similarly to embryos with cell-ECM adhesion-deficient filopodia (20), CFL1-depleted surface ectoderm cells

fail to predictably constrict their leading edge border when they reach the zippering point (Figure 6E-F). This corroborates inefficient zippering by surface ectoderm cells as the closure-limiting step leading to spina bifida in embryos conditionally lacking *Cfl1.*

Discussion

Morphogenesis normally changes tissues shapes at rates spatiotemporally coordinated with structures around them. Here we find that conditional *Cfl1* disruption causes failures to predictably achieve symmetrical shape of the cranial neural tube, and diminished rate of change in PNP shape, in embryos which develop exencephaly and spina bifida. These outcomes are probabilistically manifested as partially-penetrant phenotypes in genetically-predisposed embryos. Partial penetrance is a common feature of NTD models, which in some cases can be related to a genetic threshold effect (18, 48). During spinal neurulation, we propose that inefficient zippering reduces morphogenetic robustness such that some embryos complete closure within a tolerable timeframe, whereas others fail to close by a developmental deadline resulting in spina bifida.

The mechanisms underlying spina bifida and exencephaly are distinct in our model: neuroepithelial *Cfl1* deletion prevents Closure 2 formation cranially whereas surface ectoderm loss diminishes zippering in the spine. We cannot test whether surface ectoderm CFL1 also enhances zippering cranially due to dysmorphology of a large subset of embryos lacking its expression. However, CFL1 molecular regulation is regionally distinct, with high levels of phosphorylation (inhibition) in leading edge cells lining the hindbrain neuropore anteriorly but not in the PNP. CFL1 is known to be phosphorylated by a limited number of kinases including TESK1 (49) and LIMK (30), the latter activated by RHO/ROCK signalling. RHO/ROCK is readily amenable to pharmacological inhibition in whole embryo culture (17, 21) and we confirmed that

this pathway's activity enhances CFL1 phosphorylation in the spinal surface ectoderm. Thus, ROCK activity diminishes CFL1 activity in surface ectoderm cells which have complete zippering.

Paradoxically, we find that CFL1 protein is abundantly located (and not phosphorylated, Figure 6G) at the leading edge of spinal surface ectoderm cells where ROCK activity enhances contractility of supracellular actomyosin cables (17). One possible explanation for this apparent contradiction is that myosin-activating functions of ROCK at the cables locally sequester it away from an alternative pathway though LIMK which phosphorylates CFL1. Also unexpected is the marked de-phosphorylation of CFL1 in mitotic cells, both within the surface ectoderm and neuroepithelium. This *in vivo* observation contrasts with the finding of increased CFL1 phosphorylation in some mitotic cells in vitro (50). Loss of CFL1 did not change the proportion of mitotic surface ectoderm cells. However, previous studies demonstrate that CFL1-deficient cells may be more prone to mitotic errors and impaired nuclear integrity (51, 52), which could then cause them to apoptose, potentially accounting for the larger aggregates of apoptotic bodies which we observed in CFL1-targeted embryos.

In HeLa cells, CFL1 activity decreases cell cortical thickness in mitosis and increases cortical tension (53). We find that surface ectoderm cell border tension is not significantly affected by loss of CFL1, although cable tension tended to cluster at the higher end of the physiological range in embryos with disrupted CFL1. We have previously observed a similar pattern in embryos with equivalent deletion of *Vangl2 (18)*. Consistently high cable tension may be a compensatory mechanism which enhances PNP shortening when zippering is deficient, as we described in the cranial region of embryos with craniorachischisis (23). Actomyosin contractions are also frequently pulsatile (54), potentially accounting for the variability in cable tension observed in this and previous studies. The observations we provide of disrupted actomyosin regulation in our new model of conditional *Cfl1* deletion include visualisation of longer and

sparser F-actin fibres in surface ectoderm cells lacking CFL1, consistent with this protein's known actions (46, 55), and diminished neuroepithelial apical localisation, as previously reported in global knockout embryos (21, 35).

We provide three lines of evidence that surface ectoderm loss of CFL1 causes spina bifida: PNP morphological changes consistent with a primary zippering defect, documentation of surface ectoderm cellular abnormalities, and lack of spina bifida phenotypes when alternative Cre-drivers are used to delete *Cfl1* in the neuroepithelium (and mesoderm). The lack of spinal phenotypes in embryos lacking CFL1 primarily in the neuroepithelium was unexpected (21). We cannot exclude potential additive or synergistic effects arising from disruptions of different tissues in our *Grhl3*^{Cre} model, as previously observed in *Xenopus (56, 57)*. However, *Cdx2*^{Cre} deletes *Cfl1* first in the neuroepithelium and then in both the neuroepithelium and surface ectoderm at later stages, but only causes a low penetrance of kinked tail phenotypes consistent with delayed closure. Lack of spina bifida in the *Cdx2*^{Cre} model combined with the observed increase in PNP lengths at early somite stages in the *Grhl3*^{Cre} model further define the critical role of CFL1 in the surface ectoderm for early stages of spinal closure. This is consistent with the finding that CFL1 enhances dynamicity of filopodial protrusions, which primarily facilitate zippering at early stages of spinal closure before lamellipodia-like ruffles become more important at later stages of closure (13). Our new live imaging analysis suggests these two different types of surface ectoderm protrusions have very different dynamics. Lamellipodia-like ruffles are stable landmarks identifiable for many minutes, whereas filopodia-like protrusions rapidly extend and retract. These are distinct from the long and seemingly more stable surface ectoderm 'bridges' described during cranial closure (24), resembling bridges between *Drosophila* cardiac cells which button segments with matching adhesion molecules (58).

Diminished filopodial dynamicity may reduce zippering by impairing their 'searching' behaviour (59), pairing of new cell-ECM/cell-cell adhesions along the embryonic midline (20, 60), and/or by

interrupting maturation of the newly-fused epithelium immediately rostral to the zippering point. The sequence of CDC42/RAC1 dependent mesenchymal-like protrusive activity changing mutually-antagonistically to RHO-dependent maturation of apical cell-cell junctions is well established during epithelial maturation (27, 61, 62). CFL1 can facilitate this transition, for example by depolymerising F-actin within filopodia to facilitate their retraction (63). CFL1 also promotes turnover of focal adhesions (64, 65) and we observe key similarities between *Cfl1*-depleted surface ectoderm cells and those lacking integrin B1 (20): namely larger cell areas and impaired constriction of the leading-edge cell border at the zippering point. Loss of *Cfl1* may therefore impair zippering through dual action in surface ectoderm filopodia – diminishing their exploratory displacements to find adhesion targets and slowing turnover of cell-ECM adhesions at the embryonic midline.

In conclusion, CFL1 is ubiquitously expressed but differentially regulated through regional localisation and phosphorylation downstream of RHO/ROCK signalling during mouse neurulation (represented in Figure 6G). It regulates the F-actin cytoskeleton in both the neuroepithelium and surface ectoderm, and its non-redundant functions in the surface ectoderm are necessary for timely PNP closure. In these cells, its loss increases cell size, produces clusters of apoptotic cell debris, and diminishes the dynamicity of filopodial-like protrusions which persist abnormally even in cells which have left the advancing zipper. Embryos lacking surface ectoderm CFL1 zipper the forming neural tube at a slower speed than controls, such that a subset achieve delayed PNP closure, in some cases with kinked tail defects, while others fail to close by a developmental deadline and ultimately develop spina bifida.

Materials And Methods

Mouse transgenic alleles

All mouse lines were generated or maintained on a C57/BL6 background. Genotyping was performed by PCR on DNA extracted from ear clips. The following transgenic mouse lines were used: *Cdx2*^{Cre} (66) (gene symbol: Tg (CDX2-cre)101Erf, MGI: 3696953); *T*^{CreERT2} (67) (gene symbol: Tg (T-cre/ERT2)1Lwd, MGI: 5509185); *Grhl3*^{Cre} (68) (gene symbol: Grhl3$^{tm1\ (cre)Cgh}$, MGI: 4430902).

Mice with a conditional floxed allele of *Cfl1* (*Cfl1*$^{Fl/Fl}$) were derived from the strain C57BL/6N-Atm1Brd Cfl1tm1a (KOMP)Mbp/JMmucd (RRID:MMRRC_047079-UCD), obtained from the Mutant Mouse Resource and Research Center (MMRRC) at University of California at Davis, an NIH-funded strain repository, and was donated to the MMRRC by The KOMP Repository, UC Davis Mouse Biology Program (Stephen Murray, Ph.D., The Jackson Laboratory). Mice with the tm1a allele were crossed with flipase-expressing mice to generate the conditional tm1c allele. The flipase allele used was derived from C57BL/6N-Tg (CAG-Flpo)1Afst/Mmucd (RRID:MMRRC_036512-UCD) obtained from the MMRRC, and was donated by the MMRRC at UC Davis. The original transgenic was donated by Dr. Konstantinos Anastassiadis from Technische Universitaet Dresden.

Homozygous *Cfl1*$^{fl/fl}$ mice were crossed with Cre-heterozygous animals, to generate *Cfl1*$^{fl/+}$;*Cre/*+ animals. These were in turn crossed with *Cfl1*$^{fl/fl}$ mice to generate experimental *Cfl1*$^{fl/fl}$;*Cre/*+ embryos.

Animal procedures

All animal work was performed under the regulation of the UK Animals (Scientific Procedures) Act 1986 and the National Centre for the 3Rs' Responsibility in the Use of Animals for Medical Research (2019). Mice used for breeding and experimental mating were no less than 8 weeks and no more than 1 year of age.

Mice were mated overnight or early in the morning, and checked for a copulation plug the next morning or at midday respectively. Positive plugs found after overnight breeding were designated embryonic day (E) 0.5, while plugs found the same day were considered E0.5 from midnight.

Lineage tracing was achieved by crossing heterozygous Cre mice with *Rosa26-mTmG* mice. Time-dependent lineage tracing using the inducible $T^{CreERT2}$ mouse line was achieved by oral tamoxifen administration (10 mg/mouse) at E7.5(69). Cfl1-null alleles were generated by breeding $Cfl1^{Fl/Fl}$ with $\beta\text{-}actin^{Cre/+}$ mice(70) and back-crossing to eliminate the Cre allele.

Pregnant dams were sacrificed by cervical dislocation at appropriate embryonic stages, from E8.5 – 14.5. Individual deciduas were dissected from the uterus in warm Dulbecco's Modified Eagle's Medium containing 25 mM HEPES and 10% fetal calf serum. Embryos were then dissected free of decidua, and used for culture, fixation or laser ablation experiments.

Embryo culture

Embryo culture was performed as previously described (71). Decidua, trophoblast and Reichert's membrane layers were carefully removed, excluding the trophoblast of the ectoplacental cone and taking care not to pierce the yolk sac. Embryos were then stage matched and randomly allocated to experimental groups. Embryos were carefully added to a 30 ml culture tube with pre-warmed rat serum filtered through a 0.45 µm Millipore filter (0.5 ml per embryo). Culture tubes were gassed for 30 sec with 20% O_2, 5% CO_2, 75% N_2, sealed using vacuum grease and added to a roller culture incubator for the duration of the experiment. After cultures, embryos were processed as below for fixing.

For ROCK inhibition experiments, RHO/ROCK inhibitor (Y27632, Cambridge Biosciences SM02-1) dissolved in water was added to rat serum at a concentration of 10 µM, while control embryos were cultured in rat serum alone.

To measure the speed of zippering point progression in culture as previously described(15), a small hole was created in the yolk sac and amnion using dissection forceps, revealing the zippering point. A small volume of DiI (Invitrogen V22889) was injected lateral to the zippering point, and embryos were added to rat serum and cultured for 6.5 h. Zippering rate was calculated by: distance moved by the zippering point beyond the DiI mark, divided by elapsed time.

Embryos were fixed by removing all embryonic layers including the yolk sac and amnion washing briefly in ice cold PBS and fixed immediately in 4% PFA in PBS. Yolk sacs were also washed in PBS and kept for genotyping. Yolk sacs (embryos) or ear clips (mice) were lysed for at least 4 h at 56°C in 50 µl lysis buffer (Viagen Biotech) with 10% proteinase K. Lysates were diluted 1:10 with Milli-Q water and processed for PCR using GoTaq G2 Flexi DNA Polymerase kit (Promega). Reactions were placed in a thermocycler on a touchdown program, and subsequent amplified DNA was evaluated by gel electrophoresis.

Immunofluorescence

Primary and secondary antibodies used in this study are detailed in Supplementary Table 1. All washes and incubation steps were on a benchtop shaker. For ROCK1 and pMLC-II primary antibodies, an antigen retrieval step was included: embryos were preincubated for 15 min in sodium citrate solution (10 mM in PBS + 0.05% Tween 20, pH 6) at room temperature (RT), followed by 25 min at 90°C in fresh sodium citrate solution. Embryos were allowed to cool at RT

before proceeding to the blocking step. For all other antibodies, embryos were permeabilised in PBS + 0.1% Triton (PBST) for 1 h at RT.

After antigen retrieval or permeabilisation, embryos were incubated in blocking solution (PBST + 5% bovine serum albumin), either overnight at 4°C or for 6 h at RT. Primary antibodies were diluted in blocking solution and incubated at 4°C overnight. Primary antibodies were diluted at the following dilutions: 1;100 rabbit anti-CFL1, 1:200 rabbit anti-pCFL1, 1:100 rabbit anti-ROCK1, 1:200 mouse anti-pHH3, 1:200 rabbit anti-pMLC-II, 1:100 mouse anti-pMLC-II, 1:100 mouse anti-E cadherin, 1:200 rabbit anti-cCasp3. The following day, primary antibody solutions were removed and embryos were washed 3x in blocking solution at RT. Embryos were then incubated in secondary antibody solution for 2 h at RT. When used, DAPI and/or Phalloidin were also added during this step. Secondary antibodies were diluted in blocking solution at the following concentrations: Alexa fluor -405 and -647 secondary antibodies, 1:250; Alex fluor -488 and -568, 1:500. DAPI was diluted at 1:5000, and Phalloidin at 1:250. Finally, embryos were washed 1x 1 h in blocking solution, 1x 1 h in PBST, 1 h in PBS, and stored in PBS + 1% azide.

Confocal microscopy and laser ablation

All confocal imaging was performed using a Zeiss Examiner LSM880 confocal microscope using 10x/NA0.5/ or 20x/NA1.0 Plan Apochromat water immersion objectives. Laser power and gain settings were kept the same for embryos from a single experiment.

For laser ablation, embryos were stained, positioned and ablated as previously described(72). After dissection, yolk sacs were kept for genotyping and live embryos were stained for 5 min in 1:500 Cell Mask (Thermo Fisher Scientific) in DMEM (without FBS). The caudal half of the embryo was separated using dissection forceps, as movement caused by the heartbeat prevents accurate ablations, and positioned in a pre-warmed agarose plate with DMEM. Curved

microsurgical needles (see Supplementary Table 1) were positioned in the agarose to provide support to the tissue and keep it stable during imaging. The tissue was positioned with the dorsal side facing up; the posterior neuropore or caudal surface ectoderm was positioned as flat as possible, depending on whether the cable or surface ectoderm cells were being ablated. Cell borders were imaged in a single z plane. After 1 sec imaging, a single cell border was ablated using a MaiTai laser (710 nm wavelength, 80% laser power, 0.34 µsec pixel dwell time, 20 iterations). After the ablation, imaging continued for approximately 17 sec to capture cell and tissue recoil.

Image analysis

All image processing and analysis was carried out using FIJI(73). Images which are 'surface subtracted'(19) to selectively visualize the surface ectoderm have a homogenous, null background where there is no surface. 3D projections are generated in FIJI as 8-bit images and also have a homogenous, computer background. Brightness and contrast were adjusted evenly across all image panes. Salt-and-pepper noise was eliminated using the remove function in FIJI when appropriate. AiryScan images underwent standard processing in ZEN Blue using the manufacturer's software. The 'surface subtraction' macro used for extracting surface signal from fluorescence images is available on Github courtesy of Dale Moulding https://github.com/DaleMoulding/Fiji-Macros. All relevant data is reported in this paper and supplementary information and is available from the corresponding author.

Where possible, analyses were performed blind to genotyping or treatment group. Fluorescence intensity quantifications of an area (Figure 1G, Supplementary Figure 1C) were carried out on regions of a consistent size by measuring mean grey values. Fluorescence intensity profiles (Supplementary Figure 1B, Supplementary Figure 3B) and length measurements (Figure 2F - H,

Figure 5G, Supplementary Figure 4) were taken using the Segmented Line tool. Cell shape parameters (Figure 4 E – F, Supplementary Figure 2G, Supplementary Figure 6D) were measured using FIJI. Initial recoil of laser ablations (Supplementary Figure 6B – C) was calculated as the change in length of a line drawn between two reference points before and after the ablation(72).

Protrusions' analysis was carried out using raw z stacks. Individual protrusions were identified and recorded using the ROI manager tool. Protrusions were then tracked over time - protrusions could move in Z as well as X and Y, so they were also tracked over z slices.

Statistical analysis

Statistical analysis was performed using OriginLab and Microsoft Excel software. Statistical tests used, exact n numbers and significance are reported in figures and figure legends. Mean ± SEM (standard error of the mean) are displayed in all line graphs. Box plot lines display the median, 25th and 75th percentiles, while the square represents the mean. Two-tailed $p \leq 0.05$ was considered statistically significant. The embryo was the unit of measure except for live imaging analysis, in which individual protrusions were the unit of measure. Proportions were compared by Fisher's exact test, and means of two groups by Student's T-test.

Competing Interest

None of the authors have competing interests to declare.

Acknowledgements

This study was supported by the Wellcome Trust (211112/Z/18/Z and 211112/Z/18/A to G.L.G.). E.M. is funded by a Marie Skłodowska-Curie Actions project (101067028).

Author contributions

Conception or design of the work: GLG. Acquisition, analysis, or interpretation: GLG, ARM, AK, HC, RS, EM, NDEG, AJC. Drafting the work: GLG, ARM. Reviewing: GLG, AK, HC, RS, EM, NDEG, AJC. Final approval and agreement to be accountable: All authors.

References:

1. P. Agarwal, R. Zaidel-Bar, Principles of Actomyosin Regulation In Vivo. *Trends Cell Biol* **29**, 150-163 (2019).
2. G. H. Koenderink, E. K. Paluch, Architecture shapes contractility in actomyosin networks. *Curr Opin Cell Biol* **50**, 79-85 (2018).
3. J. R. Bamburg, H. E. Harris, A. G. Weeds, Partial purification and characterization of an actin depolymerizing factor from brain. *FEBS Lett* **121**, 178-182 (1980).
4. E. D. Goley, S. E. Rodenbusch, A. C. Martin, M. D. Welch, Critical conformational changes in the Arp2/3 complex are induced by nucleotide and nucleation promoting factor. *Mol Cell* **16**, 269-279 (2004).
5. M. Bergert, S. D. Chandradoss, R. A. Desai, E. Paluch, Cell mechanics control rapid transitions between blebs and lamellipodia during migration. *Proc Natl Acad Sci U S A* **109**, 14434-14439 (2012).
6. P. Lappalainen, T. Kotila, A. Jegou, G. Romet-Lemonne, Biochemical and mechanical regulation of actin dynamics. *Nat Rev Mol Cell Biol* **23**, 836-852 (2022).
7. S. Buracco, S. Claydon, R. Insall, Control of actin dynamics during cell motility. *F1000Res* **8** (2019).
8. L. Fort *et al.*, Fam49/CYRI interacts with Rac1 and locally suppresses protrusions. *Nat Cell Biol* **20**, 1159-1171 (2018).
9. K. Hu, L. Ji, K. T. Applegate, G. Danuser, C. M. Waterman-Storer, Differential transmission of actin motion within focal adhesions. *Science* **315**, 111-115 (2007).
10. M. J. Redd, L. Cooper, W. Wood, B. Stramer, P. Martin, Wound healing and inflammation: embryos reveal the way to perfect repair. *Philos Trans R Soc Lond B Biol Sci* **359**, 777-784 (2004).
11. G. Kanellos, M. C. Frame, Cellular functions of the ADF/cofilin family at a glance. *J Cell Sci* **129**, 3211-3218 (2016).
12. A. Wang, X. Ma, M. A. Conti, R. S. Adelstein, Distinct and redundant roles of the non-muscle myosin II isoforms and functional domains. *Biochem Soc Trans* **39**, 1131-1135 (2011).

13. A. Rolo *et al.*, Regulation of cell protrusions by small GTPases during fusion of the neural folds. *Elife* **5**, e13273 (2016).
14. E. Nikolopoulou, G. L. Galea, A. Rolo, N. D. Greene, A. J. Copp, Neural tube closure: cellular, molecular and biomechanical mechanisms. *Development* **144**, 552-566 (2017).
15. E. Nikolopoulou *et al.*, Spinal neural tube closure depends on regulation of surface ectoderm identity and biomechanics by Grhl2. *Nat Commun* **10**, 2487 (2019).
16. E. Maniou *et al.*, Caudal Fgfr1 disruption produces localised spinal mis-patterning and a terminal myelocystocele-like phenotype in mice. *Development* 10.1242/dev.202139 (2023).
17. M. B. Butler *et al.*, Rho kinase-dependent apical constriction counteracts M-phase apical expansion to enable mouse neural tube closure. *J Cell Sci* **132** (2019).
18. G. L. Galea *et al.*, Cell non-autonomy amplifies disruption of neurulation by mosaic Vangl2 deletion in mice. *Nat Commun* **12**, 1159 (2021).
19. G. L. Galea *et al.*, Vangl2 disruption alters the biomechanics of late spinal neurulation leading to spina bifida in mouse embryos. *Dis Model Mech* **11** (2018).
20. M. A. Mole *et al.*, Integrin-Mediated Focal Anchorage Drives Epithelial Zippering during Mouse Neural Tube Closure. *Dev Cell* **52**, 321-334 e326 (2020).
21. S. Escuin *et al.*, Rho-kinase-dependent actin turnover and actomyosin disassembly are necessary for mouse spinal neural tube closure. *J Cell Sci* **128**, 2468-2481 (2015).
22. G. L. Galea *et al.*, Biomechanical coupling facilitates spinal neural tube closure in mouse embryos. *Proc Natl Acad Sci U S A* **114**, E5177-E5186 (2017).
23. E. Maniou *et al.*, Hindbrain neuropore tissue geometry determines asymmetric cell-mediated closure dynamics in mouse embryos. *Proc Natl Acad Sci U S A* **118** (2021).
24. C. Pyrgaki, P. Trainor, A. K. Hadjantonakis, L. Niswander, Dynamic imaging of mammalian neural tube closure. *Dev Biol* **344**, 941-947 (2010).
25. C. D. Nobes, A. Hall, Rho, rac, and cdc42 GTPases regulate the assembly of multimolecular focal complexes associated with actin stress fibers, lamellipodia, and filopodia. *Cell* **81**, 53-62 (1995).
26. L. Van Aelst, M. Symons, Role of Rho family GTPases in epithelial morphogenesis. *Genes Dev* **16**, 1032-1054 (2002).
27. B. K. Chauhan, M. Lou, Y. Zheng, R. A. Lang, Balanced Rac1 and RhoA activities regulate cell shape and drive invagination morphogenesis in epithelia. *Proc Natl Acad Sci U S A* **108**, 18289-18294 (2011).
28. L. M. Machesky, A. Hall, Role of actin polymerization and adhesion to extracellular matrix in Rac- and Rho-induced cytoskeletal reorganization. *J Cell Biol* **138**, 913-926 (1997).
29. K. L. Guan, Y. Rao, Signalling mechanisms mediating neuronal responses to guidance cues. *Nat Rev Neurosci* **4**, 941-956 (2003).
30. N. Yang *et al.*, Cofilin phosphorylation by LIM-kinase 1 and its role in Rac-mediated actin reorganization. *Nature* **393**, 809-812 (1998).
31. T. Sumi, K. Matsumoto, Y. Takai, T. Nakamura, Cofilin phosphorylation and actin cytoskeletal dynamics regulated by rho- and Cdc42-activated LIM-kinase 2. *J Cell Biol* **147**, 1519-1532 (1999).
32. H. Aizawa *et al.*, Phosphorylation of cofilin by LIM-kinase is necessary for semaphorin 3A-induced growth cone collapse. *Nat Neurosci* **4**, 367-373 (2001).
33. T. J. Chen, S. Gehler, A. E. Shaw, J. R. Bamburg, P. C. Letourneau, Cdc42 participates in the regulation of ADF/cofilin and retinal growth cone filopodia by brain derived neurotrophic factor. *J Neurobiol* **66**, 103-114 (2006).
34. C. B. Gurniak, E. Perlas, W. Witke, The actin depolymerizing factor n-cofilin is essential for neural tube morphogenesis and neural crest cell migration. *Dev Biol* **278**, 231-241 (2005).

35. J. Grego-Bessa, J. Hildebrand, K. V. Anderson, Morphogenesis of the mouse neural plate depends on distinct roles of cofilin 1 in apical and basal epithelial domains. *Development* **142**, 1305-1314 (2015).
36. S. K. Halder *et al.*, Identification of the most damaging nsSNPs in the human CFL1 gene and their functional and structural impacts on cofilin-1 protein. *Gene* **819**, 146206 (2022).
37. H. Zhu *et al.*, Association between CFL1 gene polymorphisms and spina bifida risk in a California population. *BMC Med Genet* **8**, 12 (2007).
38. E. Jaffe, L. Niswander, Loss of Grhl3 is correlated with altered cellular protrusions in the non-neural ectoderm during neural tube closure. *Dev Dyn* **250**, 732-744 (2021).
39. S. C. P. De Castro *et al.*, Neural tube closure depends on expression of Grainyhead-like 3 in multiple tissues. *Dev Biol* **435**, 130-137 (2018).
40. D. Das *et al.*, The interaction between Shroom3 and Rho-kinase is required for neural tube morphogenesis in mice. *Biol Open* **3**, 850-860 (2014).
41. I. Kowalczyk *et al.*, Neural tube closure requires the endocytic receptor Lrp2 and its functional interaction with intracellular scaffolds. *Development* **148** (2021).
42. E. R. Brooks, M. T. Islam, K. V. Anderson, J. A. Zallen, Sonic hedgehog signaling directs patterned cell remodeling during cranial neural tube closure. *Elife* **9** (2020).
43. J. M. Brown, M. J. Garcia-Garcia, Secretory pathway calcium ATPase 1 (SPCA1) controls mouse neural tube closure by regulating cytoskeletal dynamics. *Development* **145** (2018).
44. R. Massarwa, L. Niswander, In toto live imaging of mouse morphogenesis and new insights into neural tube closure. *Development* **140**, 226-236 (2013).
45. A. T. Baldwin, J. H. Kim, J. B. Wallingford, In vivo high-content imaging and regression analysis reveal non-cell autonomous functions of Shroom3 during neural tube closure. *Dev Biol* **491**, 105-112 (2022).
46. M. Aragona *et al.*, A mechanical checkpoint controls multicellular growth through YAP/TAZ regulation by actin-processing factors. *Cell* **154**, 1047-1059 (2013).
47. H. Hashimoto, F. B. Robin, K. M. Sherrard, E. M. Munro, Sequential contraction and exchange of apical junctions drives zippering and neural tube closure in a simple chordate. *Dev Cell* **32**, 241-255 (2015).
48. I. E. Zohn, Mouse as a model for multifactorial inheritance of neural tube defects. *Birth Defects Res C Embryo Today* **96**, 193-205 (2012).
49. L. Wang, A. F. Buckley, R. F. Spurney, Regulation of cofilin phosphorylation in glomerular podocytes by testis specific kinase 1 (TESK1). *Sci Rep* **8**, 12286 (2018).
50. L. Rodriguez-Fernandez, S. Company, R. Zaragoza, J. R. Vina, E. R. Garcia-Trevijano, Cleavage and activation of LIM kinase 1 as a novel mechanism for calpain 2-mediated regulation of nuclear dynamics. *Sci Rep* **11**, 16339 (2021).
51. T. Amano, N. Kaji, K. Ohashi, K. Mizuno, Mitosis-specific activation of LIM motif-containing protein kinase and roles of cofilin phosphorylation and dephosphorylation in mitosis. *J Biol Chem* **277**, 22093-22102 (2002).
52. G. Kanellos *et al.*, ADF and Cofilin1 Control Actin Stress Fibers, Nuclear Integrity, and Cell Survival. *Cell Rep* **13**, 1949-1964 (2015).
53. P. Chugh *et al.*, Actin cortex architecture regulates cell surface tension. *Nat Cell Biol* **19**, 689-697 (2017).
54. C. G. Vasquez, M. Tworoger, A. C. Martin, Dynamic myosin phosphorylation regulates contractile pulses and tissue integrity during epithelial morphogenesis. *J Cell Biol* **206**, 435-450 (2014).
55. E. Nishida, S. Maekawa, H. Sakai, Cofilin, a protein in porcine brain that binds to actin filaments and inhibits their interactions with myosin and tropomyosin. *Biochemistry* **23**, 5307-5313 (1984).

56. N. Christodoulou, P. A. Skourides, Somitic mesoderm morphogenesis is necessary for neural tube closure during Xenopus development. *Front Cell Dev Biol* **10**, 1091629 (2022).
57. N. Christodoulou, P. A. Skourides, Distinct spatiotemporal contribution of morphogenetic events and mechanical tissue coupling during Xenopus neural tube closure. *Development* **149** (2022).
58. D. Swope, J. Kramer, T. R. King, Y. S. Cheng, S. G. Kramer, Cdc42 is required in a genetically distinct subset of cardiac cells during Drosophila dorsal vessel closure. *Dev Biol* **392**, 221-232 (2014).
59. R. K. Hylton, J. E. Heebner, M. A. Grillo, M. T. Swulius, Cofilactin filaments regulate filopodial structure and dynamics in neuronal growth cones. *Nat Commun* **13**, 2439 (2022).
60. A. Jacinto *et al.*, Dynamic actin-based epithelial adhesion and cell matching during Drosophila dorsal closure. *Curr Biol* **10**, 1420-1426 (2000).
61. C. Guilluy, R. Garcia-Mata, K. Burridge, Rho protein crosstalk: another social network? *Trends Cell Biol* **21**, 718-726 (2011).
62. E. Martin, M. H. Ouellette, S. Jenna, Rac1/RhoA antagonism defines cell-to-cell heterogeneity during epidermal morphogenesis in nematodes. *J Cell Biol* **215**, 483-498 (2016).
63. D. Breitsprecher *et al.*, Cofilin cooperates with fascin to disassemble filopodial actin filaments. *J Cell Sci* **124**, 3305-3318 (2011).
64. A. C. M. Sousa-Squiavinato, M. R. Rocha, P. Barcellos-de-Souza, W. F. de Souza, J. A. Morgado-Diaz, Cofilin-1 signaling mediates epithelial-mesenchymal transition by promoting actin cytoskeleton reorganization and cell-cell adhesion regulation in colorectal cancer cells. *Biochim Biophys Acta Mol Cell Res* **1866**, 418-429 (2019).
65. L. H. Tahtamouni, A. E. Shaw, M. H. Hasan, S. R. Yasin, J. R. Bamburg, Non-overlapping activities of ADF and cofilin-1 during the migration of metastatic breast tumor cells. *BMC Cell Biol* **14**, 45 (2013).
66. T. Hinoi *et al.*, Mouse model of colonic adenoma-carcinoma progression based on somatic Apc inactivation. *Cancer Res* **67**, 9721-9730 (2007).
67. M. J. Anderson *et al.*, TCreERT2, a transgenic mouse line for temporal control of Cre-mediated recombination in lineages emerging from the primitive streak or tail bud. *PLoS One* **8**, e62479 (2013).
68. E. Camerer *et al.*, Local protease signaling contributes to neural tube closure in the mouse embryo. *Dev Cell* **18**, 25-38 (2010).
69. D. Savery *et al.*, Refinement of inducible gene deletion in embryos of pregnant mice. *Birth Defects Res* **112**, 196-204 (2020).
70. E. N. Meyers, M. Lewandoski, G. R. Martin, An Fgf8 mutant allelic series generated by Cre- and Flp-mediated recombination. *Nat Genet* **18**, 136-141 (1998).
71. S. E. Pryor, V. Massa, D. Savery, N. D. Greene, A. J. Copp, Convergent extension analysis in mouse whole embryo culture. *Methods Mol Biol* **839**, 133-146 (2012).
72. A. R. Marshall *et al.*, "Two-photon cell and tissue level laser ablation methods to study morphogenetic biomechanics" in Cell Polarity Signaling. Methods in Molecular Biology. (2022), vol. 2438.
73. J. Schindelin *et al.*, Fiji: an open-source platform for biological-image analysis. *Nat Methods* **9**, 676-682 (2012).

Figures and Legends

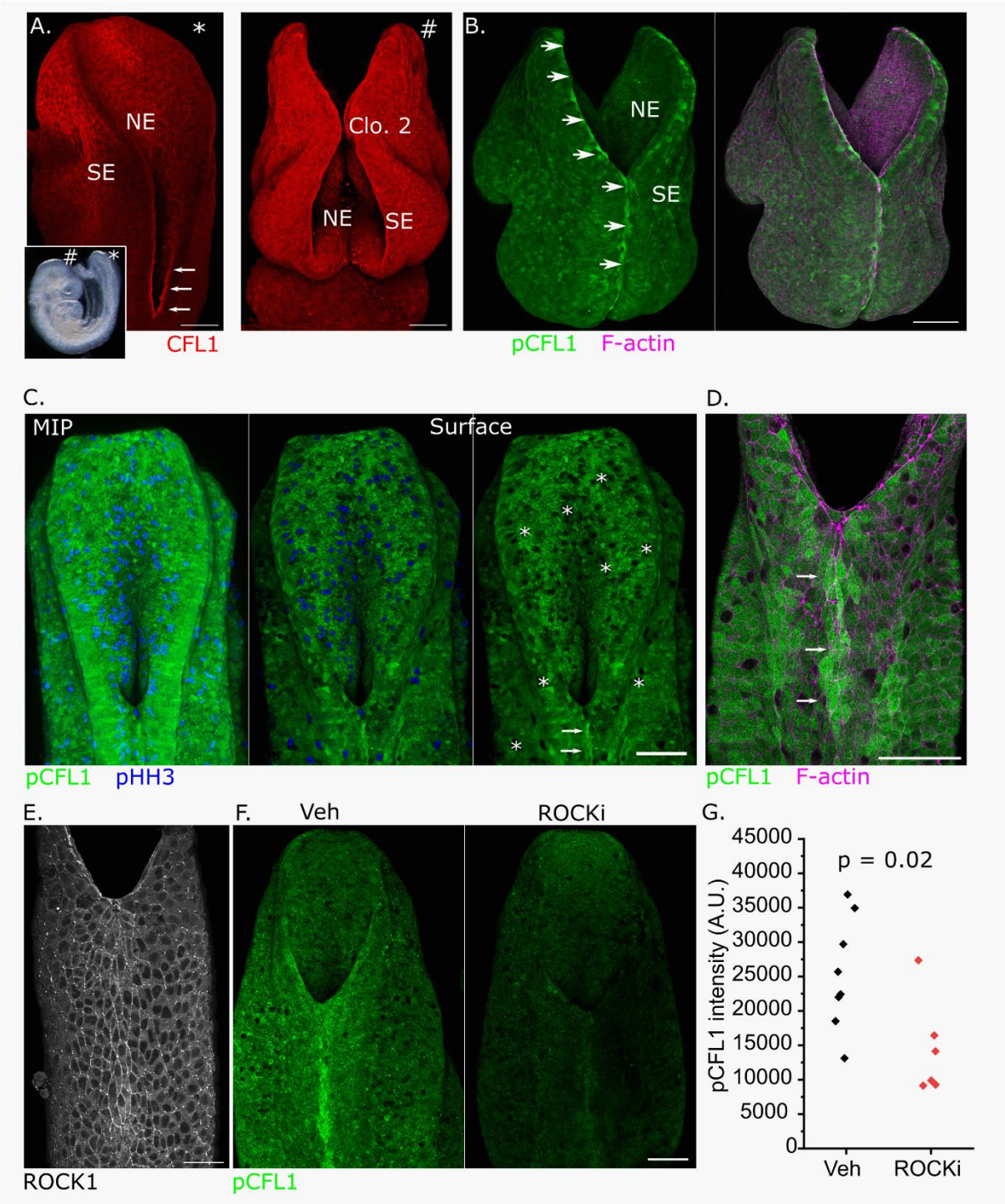

Figure 1: Regional localisation and repression of CFL1 in the surface ectoderm and neuroepithelium of mouse embryos during neural tube closure.

A. CFL1 immunolocalisation around the PNP (*) and closing cranial neural tube (#) of an 11-somite mouse embryo. The position where closure 2 (Clo. 2) would form is annotated. Arrows indicate bright CFL1 localisation immediately caudal to the zippering point of the PNP.

B. pCFL1 and F-actin localisation around the closing cranial neural tube of a 12-somite embryo. Arrows indicate the recently-closed neural tube at the embryonic midline over the forebrain and margin of the midbrain neural folds along the hindbrain neuropore.

C. Maximum intensity projection (MIP) and surface-subtracted projections (19) of pCFL1 and pHH3, illustrating diminished pCFL1 in mitotic cells (*) and bright enrichment in surface ectoderm cells at the caudal embryonic midline of a 17-somite stage embryo.

D. Surface projection of pCFL1 and F-actin in surface ectoderm cells rostral to the zippering point, showing bright, diffuse pCFL1 in a column of rostrocaudally elongated cells at the caudal midline (arrows) of a 19-somite stage embryo.

E. ROCK1 immunolocalisation in an equivalent region to (D) of a 21 somite stage embryo.

F-G. pCFL1 wholemount visualisation (F) and intensity quantification (G) in embryos cultured for 4 hours in vehicle or RHO/ROCK inhibitor (ROCKi). Points represent individual embryos, p value by T-test. A.U. = Airy units.

NE neuroepithelium, SE surface ectoderm, scale bars = 100 µm.

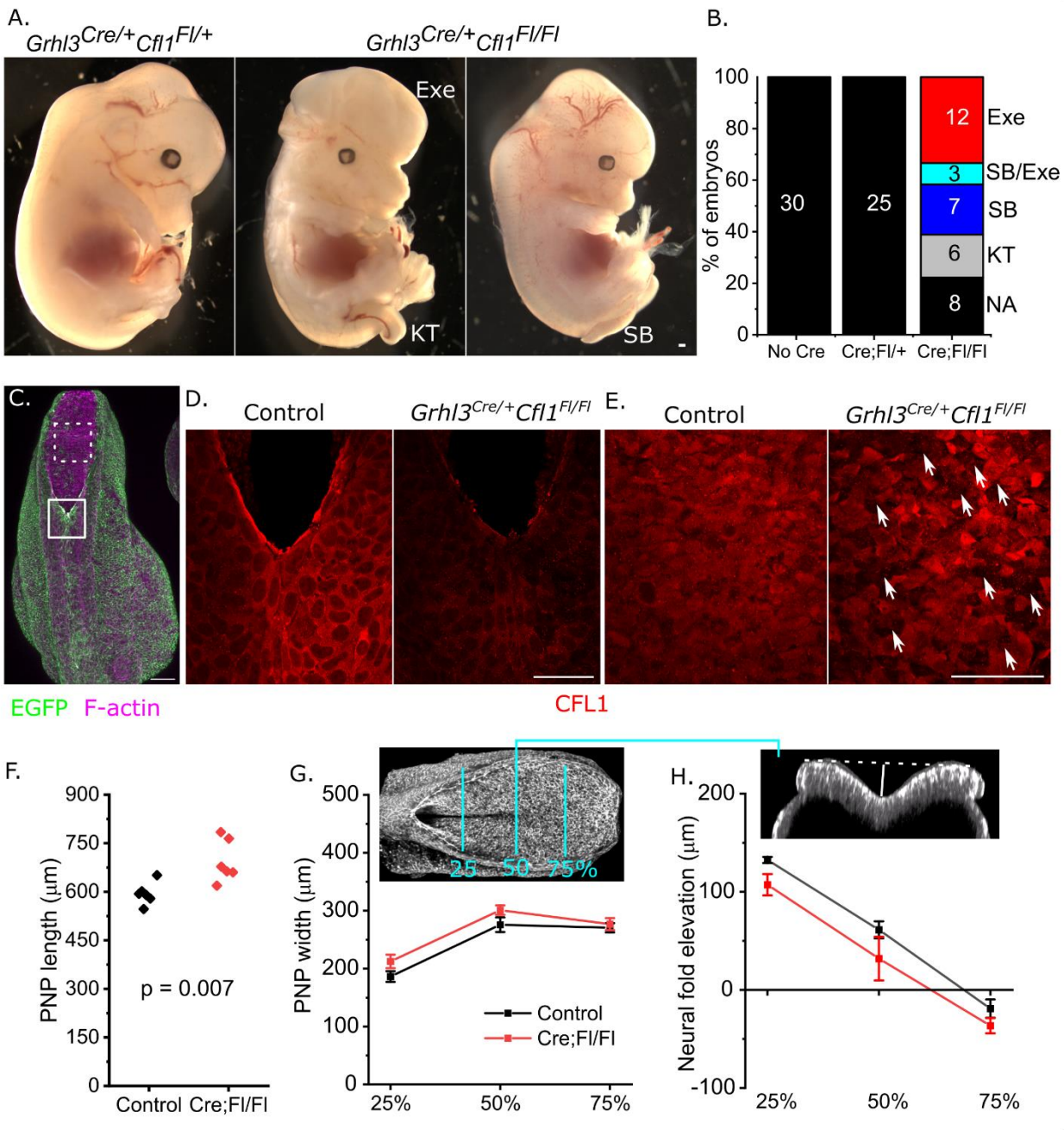

Figure 2: *Grhl3*^{Cre} deletion of *Cfl1* causes partially penetrant neural tube defects.

A. Brightfield images of E14.5 control and *Grhl3*$^{Cre/+}$*Cfl1*$^{Fl/Fl}$ (Cre;Fl/Fl) fetuses with exencephaly (Exe), spina bifida (SB), or isolated kinked tail (KT).

B. Quantification of the proportion of Cre;Fl/Fl embryos with the indicated neural tube defects. NA: no abnormality.

C. Lineage trace of *Grhl3*^{Cre} recombination (EGFP) using the mTmG reporter in the caudal region of a 22-somite embryo. The solid box indicates the zippering point (equivalent to panel D) and dashed box shows the PNP neuroepithelium (equivalent to panel E).

D-E. Surface-subtracted projections of the surface ectoderm rostral to the caudal zippering point (D) and PNP apical neuroepithelium (E) in control and Cre;Fl/Fl embryos with 16-19 somites. Surface ectoderm shows generalised reduction in CFL1 expression (D) whereas PNP neuroepithelium contains individual cells with greatly diminished apical CFL1 (arrows), consistent with mosaic deletion (E). Note the enrichment of CFL1 at surface ectoderm leading edge ahead of the zippering point in the control (as in Figure 1, quantified in Supplementary Figure 1B).

F. PNP length differs significantly between 20-25 somite stage control and Cre;Fl/Fl embryos. Points represent individual embryos;, p value by T-test.

G-H. Quantification of PNP width (G) as indicated by the cyan lines in the insert and neural fold elevation (H) indicated by the arrow, measured at 25%, 50% and 75% of the PNP's length. The same embryos as in (F) were analysed. Points represent the mean ± SEM.

Scale bars = 100 µm.

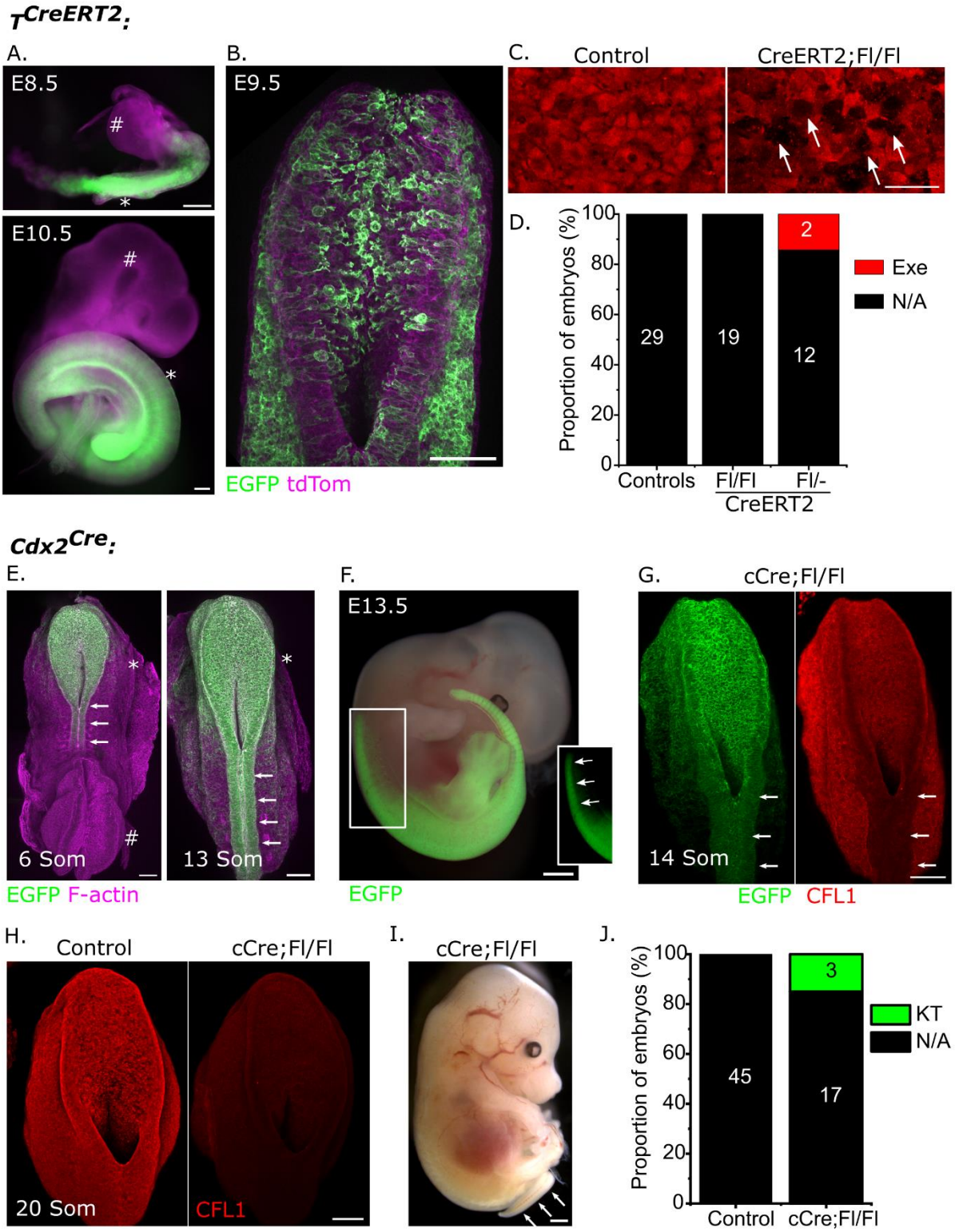

Figure 3: Neuroepithelial deletion of *Cfl1* does not cause spina bifida.

A-B. Endogenous fluorescence images lineage-tracing *T*^{CreERT2} using the mTmG reporter in embryos administered tamoxifen at E7.5 and collected at the indicated stages. EGFP indicates Cre-recombined cells in the trunk (*) but not head (#). Note mosaic neuroepithelial recombination in the PNP confocal image (B). Scale bars = 100 µm.

C. Surface projections of the PNP neuroepithelium of 15-16 somite-stage control and *T*^{CreERT2}*Cfl1*$^{Fl/Fl}$ embryos showing mosaic neuroepithelial deletion of CFL1 (arrows). Scale bar = 25 µm.

D. Proportions of neural tube defect phenotypes observed in control, *T*^{CreERT2}*Cfl1*$^{Fl/Fl}$ and *T*^{CreERT2}*Cfl1*$^{Fl/-}$ embryos.

E. Endogenous fluorescence confocal images lineage-tracing *Cdx2*^{Cre} (cCre) using the mTmG reporter showing early and persistent neuroepithelial recombination (EGFP), but later recombination in other tissues including the surface ectoderm. Spinal (*) and cranial (#) neural tube regions are indicated. Scale bars = 100 µm.

F. Endogenous fluorescence images lineage-tracing *Cdx2*^{Cre} in an E13.5 embryo showing selective recombination in the spinal cord (arrows in insert) along the thorax. Scale bar = 500 µm.

G. MIP projection showing wholemount immunolocalisation of CFL1 and endogenous EGFP from the mTmG reporter in a 14-somite *Cdx2*$^{Cre/+}$*Cfl1*$^{Fl/Fl}$*Rosa26*$^{mTmG/+}$ embryo. Arrows indicate reduced CFL1 immunofluorescence in the neural tube. Scale bar = 100 µm.

H. MIP projection showing wholemount 32mmunolocalization of CFL1 in 20-somite control and *Cdx2*$^{Cre/+}$*Cfl1*$^{Fl/Fl}$ (cCre;Fl/Fl) embryos. By this stage, CFL1 expression is reduced in all tissues. Scale bar = 100 µm.

I. Brightfield image of an E14.5 *Cdx2*$^{Cre/+}$*Cfl1*$^{Fl/Fl}$ fetus with kinked tail. Scale bar = 500 µm.

J. Proportions of neural tube defect phenotypes observed in control and *Cdx2*$^{Cre/+}$*Cfl1*$^{Fl/Fl}$ embryos.

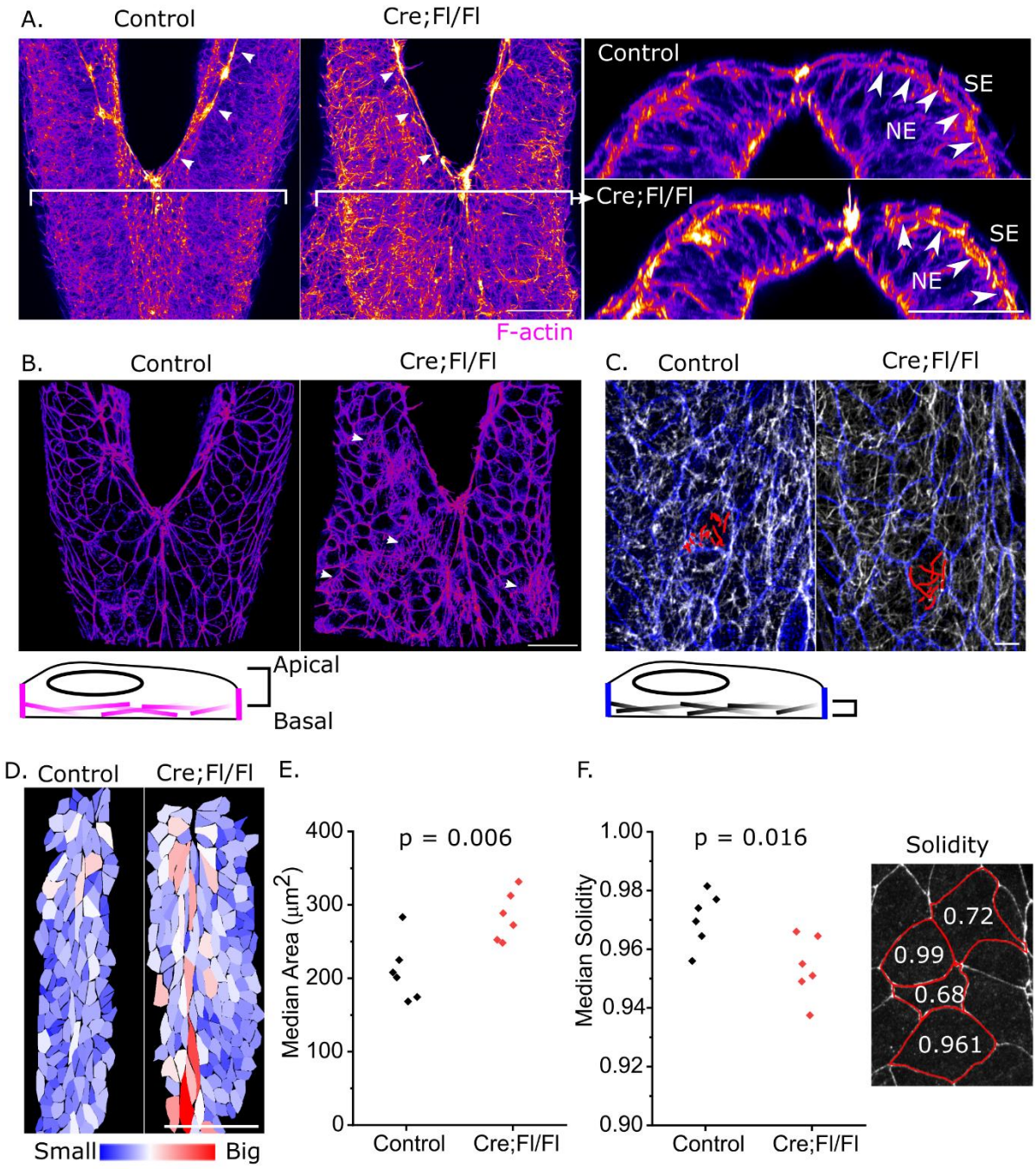

Figure 4: Cytoskeletal regulation by CFL1 influences surface ectoderm cell shape.

A. MIP projection of F-actin (Fire LUT) in 18-somite control and *Grhl3*$^{Cre/+}$*Cfl1*$^{Fl/Fl}$ embryos. Arrows indicate the surface ectoderm F-actin cables which line the PNP. Brackets indicate the position of optical cross-sections from the same images shown on the right. Arrowheads on the

optical cross-sections indicate dense F-actin networks between the basal surfaces of the surface ectoderm (SE) and underlying neuroepithelium (NE).

B. 3D reconstruction of a surface projection of the same embryos as in A. The schematic of an epithelial cell below the image illustrates the approximate thickness of the surface ectoderm visualised relative to the basal accumulation of F-actin. Arrows indicate cells with abnormal, stress fibre-like accumulations of F-actin.

C. Selective surface projection of the basal region of surface ectoderm cells in control and Cre;Fl/Fl embryos pseudo-coloured to show F-actin structures (blue cell cortex, grey stress fibres). Red lines outline the main F-actin organisations visible in exemplar cells. The schematic shows the approximate region of each cell visualised.

D. Heatmap indicating the projected area of surface ectoderm cells immediately rostral to the zippering point (at the top of the image) from control and Cre;Fl/Fl embryos.

E-F. Quantification of surface ectoderm area (E) and solidity (F) in 15-20 somite stage control and Cre;Fl/Fl embryos. Points represent individual embryos, p values by T-test. The insert illustrates surface ectoderm cells with different solidities (ZO1 label).

Scale bars A-B = 100 µm, C = 10 µm.

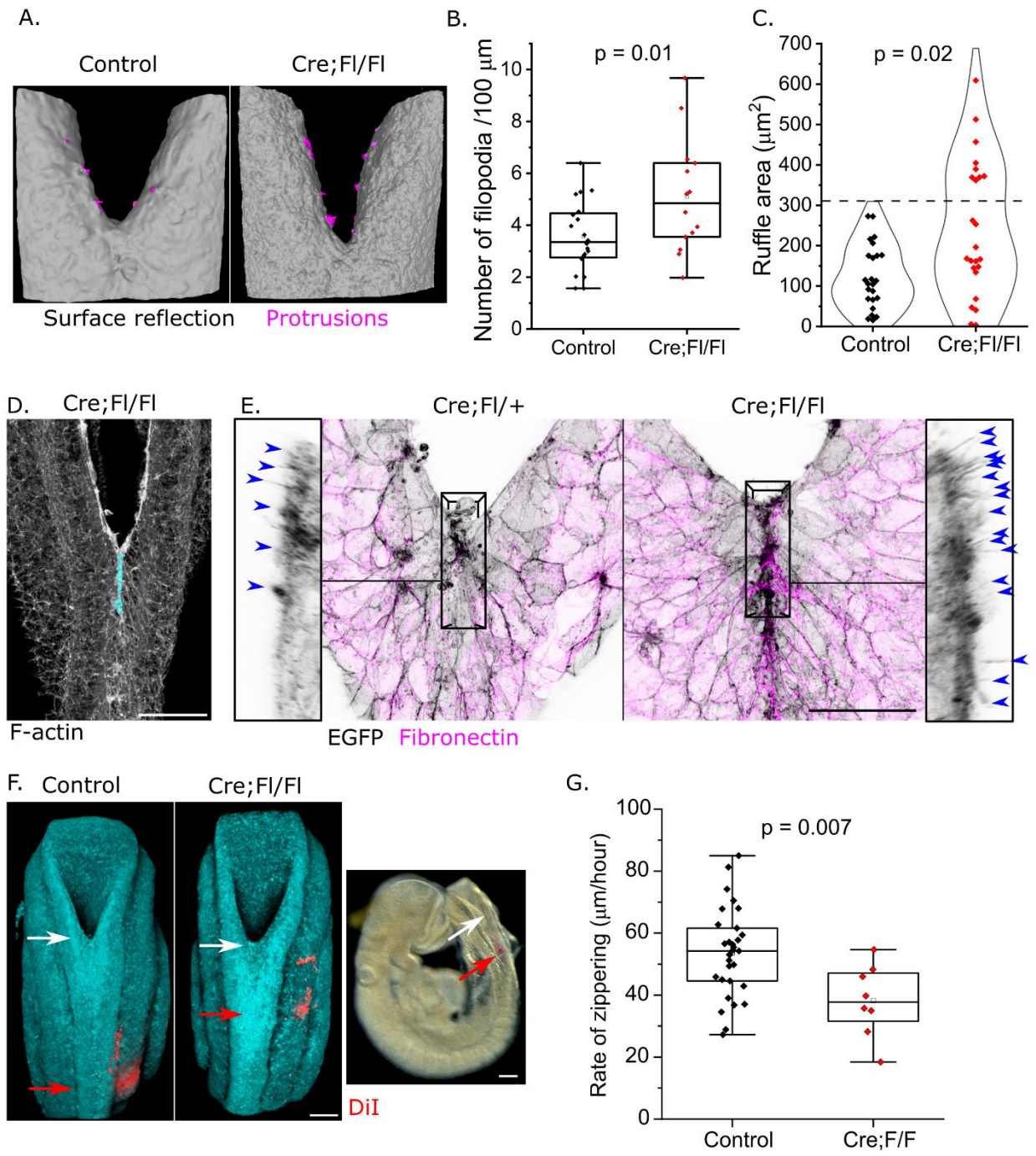

Figure 5: Surface ectoderm deletion of *Cfl1* increases the number of filopodia-like protrusions around the caudal zippering point and decreases zippering rate.

A. 3D reconstruction of reflection-imaged zippering points with pseudo-coloured protrusions in control and Cre;Fl/Fl embryos.

B. Quantification of the number of filopodia-like protrusions in control and Cre;Fl/Fl embryos with 15-20 somites. Points represent individual embryos, p value by t-test.

C-D. Quantification of the area of F-actin stained ruffles rostral to the zippering point, shaded cyan in (D), in 15-22 somite stage control and Cre;Fl/Fl embryos. Points represent mean values for individual embryos, p value by Man Whitney U test. Note that 8/24 Cre;Fl/Fl embryos exceed the range observed in controls. Scale bar = 100 µm.

E. MIP visualisation of fibronectin and surface ectoderm cell membranes lineage-traced with the mTmG reporter in control *Grhl3*$^{Cre/+}$*Cfl1*$^{Fl/+}$*Rosa26*$^{mTmG/+}$ and littermate *Grhl3*$^{Cre/+}$*Cfl1*$^{Fl/Fl}$*Rosa26*$^{mTmG/+}$ embryos. The black rectangular outline denotes the region shown in lateral projections adjacent to the main dorsal projection images. Cyan lines indicate dorsally-pointing filopodia-like protrusions visualised using the surface ectoderm EGFP lineage trace. Scale bar = 50 µm.

F. Reflection confocal imaging showing the location of the zippering point (white line) after 6 hours of culture following injection of a DiI location mark (red line). The brightfield image of a Cre;Fl/Fl embryo shows the region zippered relative to the whole embryo. The distance between the red and white arrows indicate the distance zippered. Scale bar = 100 µm.

G. Quantification of the distance zippered during the culture period in control and Cre;Fl/Fl embryos. Embryos had 18-25 somites at the end of culture and we observed no correlation between somite number and zippering rate in either genotype (not shown). Points represent individual embryos, p value by T-test.

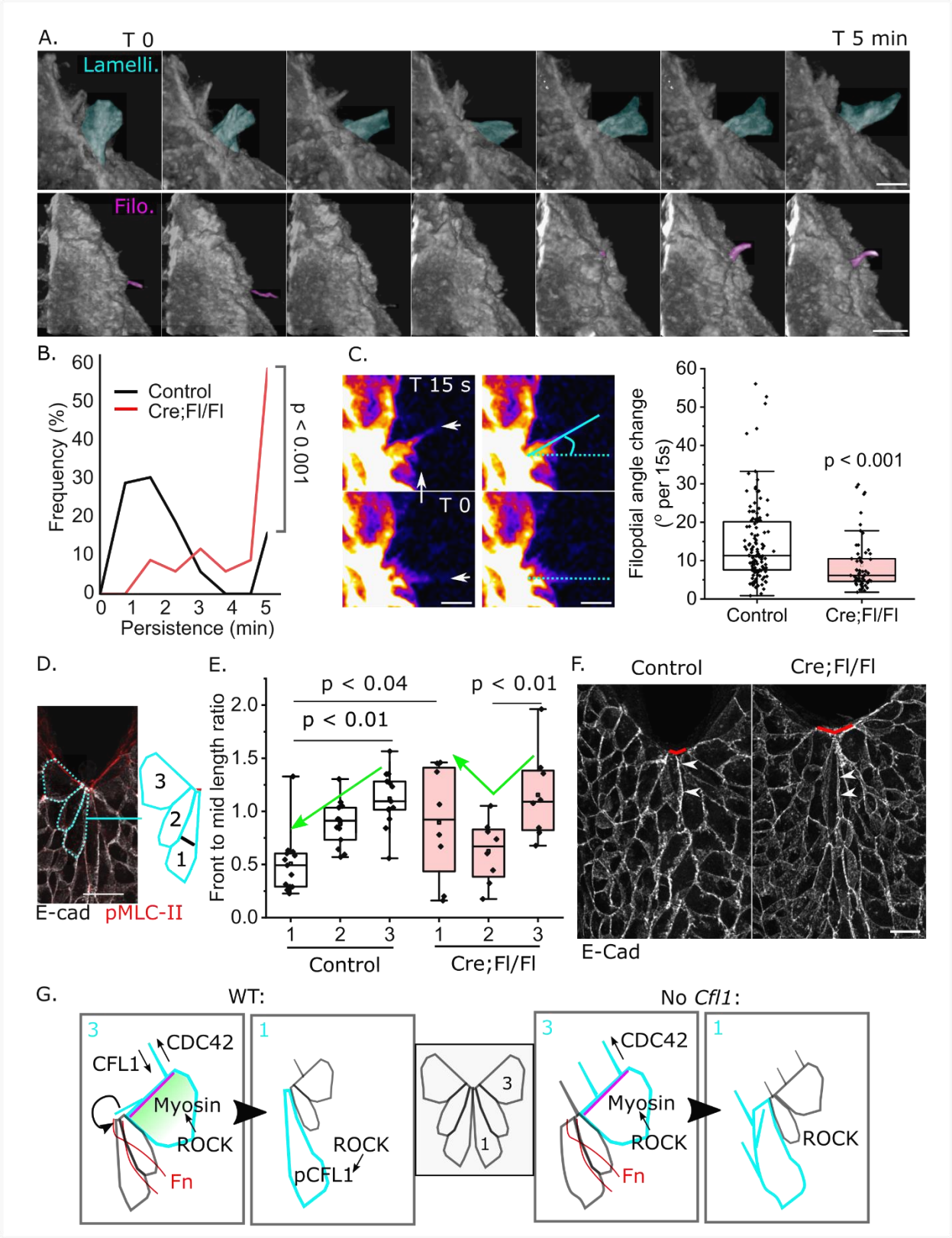

Figure 6: Filopodia-like protrusions are usually more transient than lamellipodia-like

ruffles, but are less dynamic in surface ectoderm cells lacking CFL1.

A. Live-imaged visualisation of broad lamellipodia-like ruffles (cyan pseudo-colour) and filopodia-like protrusions (pink) close to the zippering point of a 17-somite stage embryo.

B. Frequency plot of the observed duration of filopodia in control (69 protrusions from 11 embryos) and Cre;Fl/Fl (34 protrusions from 7 embryos) embryos. Protrusions which were present at the start of imaging, or which first became visible during imaging and persisted until the last timepoint of the 5-minute imagine period, were excluded from analysis. P value represents a Chi Squared comparison of the proportion of protrusions visible ≥5 minutes (Kolmogoroz-Smirnov comparison of distributions also $p < 0.001$).

C. Illustration and quantification of the change in angle of individual filopodia (arrows) calculated between each 15 s imaging interval (cyan bracket) and averaged over the lifetime of the filopodium. Points represent 128 filopodia from 11 control and 62 filopodia from 8 Cre:Fl/Fl embryos, $p < 0.001$ by T-test.

D. Illustration of the sequential constriction of neuropore-facing surface ectoderm cell borders at sequential positions (3 to 1) towards the zippering point. Position 1 is occupied by the two cells (left and right) with the most medial connections to the zippering point. Border constriction was quantified as the ratio between the cell's free border (red line) versus its width midway along its length (black line).

E. Quantification of surface ectoderm border constriction ratios in surface ectoderm cells at positions 1 to 3 in control ($n = 14$) and Cre;Fl/Fl ($n = 9$) 15-20 somite stage embryos. Two-way ANOVA p value for genotype $p = 0.003$ and position (1 to 3) $p < 0.001$, post-hoc T-tests indicated on the graph. Points present individual embryos analysed blinded to genotype.

F. E-cadherin labelled surface ectoderm cells at the zippering point in a control and Cre;Fl/Fl embryos. Red lines approximate the free border length of midline cells (position 1). Note new cell-cell junctions have formed at the embryonic midline (arrows) despite lack of *Cfl1.*

G. Schematic of proposed zippering mechanisms. Outlines represent surface ectoderm cells at the zippering point facing the neuropore margin. CFL1 is selectively enriched at the leading edge of surface ectoderm cells at the neuropore margin (green shading). These cells assemble high tension actomyosin cables (magenta) dependent on ROCK activity and extend filopodia-like protrusions (cyan) dependent on CDC42. We propose that CFL1 promotes dynamic displacement and retraction of filopodia which do not find an adhesion substrate. Adhesion depends on integrin-fibronectin contacts at the zippering point (curved arrow). Once these new connections are made, the cell constricts its neuropore-facing cell border, ROCK activity tunes down its CFL1 activity through phosphorylation. In surface ectoderm cells lacking CFL1, ROCK still activates actomyosin cable contractility, fibronectin is still assembled, and filopodia are still produced, but their turnover is inefficient, diminishing zippering speed.

Scale bars A-C = 10 µm, D-F = 20 µm.